Atmospheric
Chemistry
and Physics

Lifetime and production rate of NO$_x$ in the upper stratosphere and lower mesosphere in the polar spring/summer after the solar proton event in October–November 2003

F. Friederich[1], T. von Clarmann[1], B. Funke[2], H. Nieder[1], J. Orphal[1], M. Sinnhuber[1], G. P. Stiller[1], and J. M. Wissing[3]

[1]Karlsruhe Institute of Technology, Institute for Meteorology and Climate Research, Karlsruhe, Germany
[2]Instituto de Astrofísica de Andalucía, CSIC, Granada, Spain
[3]FB Physik, University of Osnabrück, Osnabrück, Germany

Correspondence to: F. Friederich (felix.friederich@kit.edu)

Abstract. We present altitude-dependent lifetimes of NO$_x$, determined with MIPAS/ENVISAT (the Michelson Interferometer for Passive Atmospheric Sounding/the European Environment Satellite), for the Southern polar region after the solar proton event in October–November 2003. Between 50° S and 90° S and decreasing in altitude they range from about two days at 64 km to about 20 days at 44 km. The lifetimes are controlled by transport, mixing and photochemistry. We infer estimates of dynamical lifetimes by comparison of the observed decay to photochemical lifetimes calculated with the SLIMCAT 3-D Model. Photochemical loss contributes to the observed NO$_x$ depletion by 0.1 % at 44 km, increasing with altitude to 45 % at 64 km.

In addition, we show the correlation of modelled ionization rates and observed NO$_x$ densities under consideration of the determined lifetimes of NO$_x$, and calculate altitude-dependent effective production rates of NO$_x$ due to ionization. For that we compare ionization rates of the AIMOS data base with the MIPAS measurements from 15 October–31 December 2003. We derive effective NO$_x$-production rates to be applied to the AIMOS ionization rates which range from about 0.2 NO$_x$-molecules per ion pair at 44 km to 0.7 NO$_x$-molecules per ion pair at 62 km. These effective production rates are considerably lower than predicted by box model simulations which could hint at an overestimation of the modelled ionization rates.

1 Introduction

During the maximum of the 11-yr solar magnetic activity cycle, solar flares and coronal mass ejections (CME) are most frequent. During a CME, solar plasma is ejected into space, driving a shock front that can effectively accelerate particles. Propagating along the interplanetary field lines, the energetic particles (protons, electrons and a few more massive ions) may reach the Earth and precipitate – guided by the terrestrial magnetic field – in the polar cap regions where they cause ionization in the mesosphere and stratosphere. This so-called Solar Proton/Particle Event (SPE) may also be followed by a geomagnetic storm as soon as the CME hits the geomagnetic field, forcing precipitation of low energetic particles and ionization in the upper atmosphere. We will concentrate mostly on the high-energetic particles from the SPE and their follow-ups: excitation, ionization, and dissociation of molecules. These particles have influence on the chemical composition, temperature, and dynamics of the earth's atmosphere (e.g. Crutzen et al., 1975; Jackman et al., 2001, 2007).

Different studies have parameterized the produced N-atoms by ion pair. Porter et al. (1976) calculated relativistic electron and proton impact cross sections and found that 1.25 N-atoms are produced by each ion pair, partitioned in 0.55 N(^{4}S) and 0.70 N(^{2}D). In addition to this, Rusch et al. (1981) also considered a simple ion chemistry model and found a NO$_x$-production rate between 1.3 and 1.6. The branching ratio of 80 % for the production of N(^{2}D) is from fitting a model. Baumgaertner et al. (2010) found altitude-dependent N-production rates between 0.0 and 0.3, and NO-production

rates between 0.2 and 1.2 by fitting a complex chemistry-climate model to MIPAS observation data.

By the reactions

$$N(^4S) + O_2 \rightarrow NO + O \tag{R1}$$

$$N(^2D) + O_2 \rightarrow NO + O \tag{R2}$$

NO is produced. Reaction (R2) is virtually immediate. Thus, models typically assume a production of NO and N(^{4}S). NO is also produced directly via various complex ion chemistry reactions. This is discussed, e.g., in Sinnhuber et al. (2012).
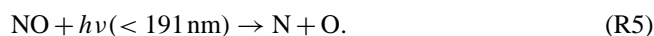
At sunset NO is converted into NO$_2$ below 70 km:

$$NO + O_3 \rightarrow NO_2 + O_2, \tag{R3}$$

which reverts at sunrise to NO by

$$NO_2 + h\nu \rightarrow NO + O. \tag{R4}$$

NO can also be dissociated by photolysis:

$$NO + h\nu(< 191\,nm) \rightarrow N + O. \tag{R5}$$

The predominant process of decomposition of NO$_x$ (N, NO, NO$_2$) is

$$N(^4S) + NO \rightarrow N_2 + O, \tag{R6}$$

which occurs in the stratosphere and lower mesosphere during the daytime because N(^{4}S) is produced by photolysis, as opposed to Reaction (R1). In our study, we distinguish between the photolytical loss due to Reaction (R5) and the photochemical loss due to Reactions (R5) and (R6). Depending on whether Reaction (R1) or Reaction (R6) dominates, photochemical loss can vary between zero and two NO per photon. Because of Reaction (R6), following relation applies to the production p:

$$1.25 = p(N(^4S) + N(^2D)) > p(NO + NO_2). \tag{1}$$

The impact of the so-called Halloween SPE in October–November 2003 on NO$_x$ has been investigated in a few studies (Seppälä et al., 2004, 2007; Jackman et al., 2005; López-Puertas et al., 2005; Baumgaertner et al., 2010; Funke et al., 2011). Model-measurement comparisons have revealed several discrepancies, but facing the complexity of the models it is not always easy to isolate the responsible process for the model-measurement difference. To this end, we use effective NO$_x$-production rates and lifetimes as model diagnostics and provide these data based on MIPAS measurements. Because the Halloween SPE is the strongest of such events MIPAS has measured in middle atmospheric NO$_x$ production (Jackman et al., 2008), we use it as an experimental examination of the altitude-dependent NO$_x$-production rates and lifetimes of NO$_x$.

We focus on altitudes between 42 km and 64 km, because this region is both affected by the SPE and covered by MIPAS observations. While the lifetime of NO and NO$_2$ is shorter than a day due to Reactions (R3) and (R4), the lifetime of NO$_x$ is typically a few days at altitudes from 42 km to 64 km at sunlit conditions (Brasseur and Solomon, 2005). So the multitude of MIPAS/ENVISAT measurements per day allows to determine the lifetime of NO$_x$ in the middle atmosphere impacted by a SPE. We analyze these lifetimes in a first step (Sect. 3.1). With these altitude-dependent lifetimes available, the dependence of the NO$_x$ production on the ion production rate is estimated (Sect. 3.2). Downward transport of upper atmospheric air into the upper stratosphere and lower mesosphere has a huge impact on NO$_x$ in the winter hemisphere (Siskind and Russell, 1996; Funke et al., 2005b; Randall et al., 2007). That air intrudes in the mesosphere and elevates the volume mixing ratio (vmr) of NO$_x$ about some orders of magnitude. Smaller enhancements due to the EEP impact cannot be easily distinguished from the descending NO$_x$-rich air masses. Thus, we analyze only data from the Southern Hemisphere where vertical motion is upward during the period under investigation and descended NO$_x$-rich air masses from the previous winter have already disappeared. We compare our results to studies which have also estimated the ion production rate in Sect. 4.

Ionization rates are provided by the Atmospheric Ionization Module Osnabrück (AIMOS). Data of MIPAS are described in Sect. 2.1, AIMOS is described in Sect. 2.2. Data analysis is shown in Sect. 3.

2 Used data

In this section, we describe the data used for this study. Mixing ratios of NO and NO$_2$ are retrieved from spectra of MIPAS (Sect. 2.1) and the 3-D model AIMOS is used to get ionization rates (Sect. 2.2).

2.1 MIPAS/ENVISAT

The Michelson Interferometer for Passive Atmospheric Sounding (MIPAS, Fischer et al., 2008) on the European Environment Satellite (ENVISAT) has recorded limb emission spectra since 2002. ENVISAT has a sun-synchronous orbit with an inclination of 98° at an altitude of about 800 km (783 km since 2010). All latitudes up to ±90° can be observed both at day and at night at about 10:00 a.m. and 10:00 p.m. local time, respectively. We use NO$_x$-data of the nominal measurement mode (Funke et al., 2005a), which covers altitudes from 6–68 km. MIPAS records limb emission spectra in the infrared wave range (4.1–14.7 µm). The NO fundamental band at 5.3 µm and the NO$_2$ fundamental ν_3 band at 6.2 µm are used to determine the vmr profiles of NO and NO$_2$. Additional quantities available from the retrieval for each geolocation are the temperature T [K], the pressure p [hPa], volume mixing ratio and the averaging kernel (AVK).

NO and NO$_2$ are products of the Institute of Meteorology and Climate research (IMK) and of the Instituto

de Astrofísica de Andalucía (IAA). Both trace gases are available for the full mission period (with exception of April–December 2004). We used version V3O_NO_14 and V3O_NO2_13/14 which has substantially improved with respect to the retrieval setup described in Funke et al. (2005a) by (i) the use of log(vmr) instead of vmr in the retrieval vector, (ii) a revised correction scheme for line of sight variations of the NO$_x$ partitioning close to the terminator, and (iii) joint-fitted vmr horizontal gradients at constant longitudes and latitudes (Funke et al., 2011). Because there is a lot NO in the 110 km region which is in the line-of-sight of every limb scan, the data are corrected for by joint-fitting the thermospheric column. The accuracy of stratospheric and mesospheric NO and NO$_2$ data is better than 15 % (Funke et al., 2005a).

In the analysis, we calculate zonal averages of vmr and the number density n ($\overline{\mathrm{vmr}}$ and $\overline{n}$) of the polar cap between 50° S and 90° S. We only take $\overline{\mathrm{vmr}}$ and $\overline{n}$ into account, when there are at least measurements from three geolocations and when the arithmetic mean of the AVK diagonal elements $\overline{\mathrm{AVD}}$ is greater than 0.03. When $\overline{\mathrm{AVD}}$ is smaller than 0.03, $\overline{\mathrm{vmr}}$ depends strongly on its a priori value of the retrieval. The six-hour zonal means of the vmr we use in Sect. 3.1 are calculated using data from maximum of 61 geolocations. During the SPE, the number of geolocations used is reduced to about 35–40 on most days. The standard error of the mean is dependent on the number of geolocations and thus bigger during the SPE but mostly lower than 10 %. The 24-h zonal means of the NO$_x$ number density we use in Sect. 3.2 are calculated by maximum 211 geolocations and mostly more than 150 geolocations. The standard error of the mean is always lower than 1 %, besides at the days during the SPE (lower than 5 %).

2.2 AIMOS

The Atmospheric Ionization Module Osnabrück, (AIMOS, Wissing and Kallenrode, 2009) is a 3-D model, which determines the atmospheric ionization caused by protons, electrons, and alpha particles. It is based on flux measurements of GOES (Geostationary Operational Environmental Satellite) and POES (Polar Operational Environmental Satellite) covering an energy range of 150 eV to 500 MeV for protons, 4 MeV to 500 MeV for alpha particles, and 150 eV to 2.5 MeV for electrons. In addition, the energy range of the electrons is extrapolated to 5 MeV. AIMOS provides ionization rates from 2002 until 2010, which depend on altitude, latitude and longitude. The spatial resolution is $3.6° \times 3.6°$ with 67 pressure levels, ranging from 10^5 Pa to 1.7×10^{-5} Pa. The temporal resolution is two hours. The unit of the ionization rates is cm^{-3} s^{-1}.

3 Data analysis

This section presents the procedure of the data analysis used for our investigation. The determinations of the lifetimes and the dependence of NO$_x$ on the ion pair production (IPP) are shown in Sects. 3.1 and 3.2, respectively.

3.1 Lifetime of NO$_x$

The SPE in October–November 2003 induced a large increase of the NO$_x$ vmr in polar latitudes above $\sim$45 km which was observed, for example, by MIPAS on ENVISAT (López-Puertas et al., 2005). The volume mixing ratio of NO$_x$ has its maximum on 30 October. Subsequently, there is a decrease lasting for four days. We average MIPAS data of each retrieved altitude separately (42 km, 43 km, 44 km, 45 km, 46 km, 47 km, 48 km, 49 km, 50 km, 52 km, 54 km, 56 km, 58 km, 60 km, 62 km, and 64 km) at the Southern polar cap (between 50° S and 90° S) over a time period of six hours to get a smoothed vmr gradient. Then we fit an exponential function

$$\mathrm{vmr}(t) = \mathrm{vmr}(t_0) \cdot \exp\left(-\frac{t - t_0}{\tau}\right) + \mathrm{const.} \tag{2}$$

to the data after the maximum of vmr. t_0 denotes the time of the maximum of vmr. τ is the lifetime of NO$_x$, which depends on altitude. Consequently, the fit has three degrees of freedom (vmr(t_0), τ, const). Figure 1 shows 6 h-averaged MIPAS measurements with the standard error of the mean (error bars) at altitudes of 45 km and 62 km. The exponential fit to the data vmr(t) is computed by weighting each value with its inverse variance. τ and the 1σ-range of τ are shown in Fig. 2 (left) for all altitudes. The corresponding reduced residuals (χ^2) between measurement and fit are shown on the right. They vary between 0.3 and 1.4. χ^2 values lower than one show on the one hand that the assumption of an exponential decay is reasonable. On the other hand they are an evidence that the standard error of the mean is overestimated by using the familiar estimator function (Toohey et al., 2011). When χ^2 becomes higher, it is more likely that the fit is outside the error bars of some values.

The lifetime as calculated from MIPAS data depends on the altitude-dependent photolysis rate, the reaction rate of Reaction (R6), and on a dynamic part due to horizontal transport and mixing. There is no strong NO upwelling or downwelling in polar summer. Horizontal transport and mixing are responsible for a distribution of NO$_x$ towards latitudes outside the polar cap. In our idealised assumption, the source of NO$_x$ is inside the polar caps due to the SPE and there is no NO$_x$ enhancement outside the polar caps nor any important change of the usual NO$_x$ production without SPE during the three days after the SPE. In particular, there is no enhanced particle precipitation during these days at 42–64 km altitude. So we can assume an exponential decay not only for the loss due to photochemistry but also for dilution due to dynamics.
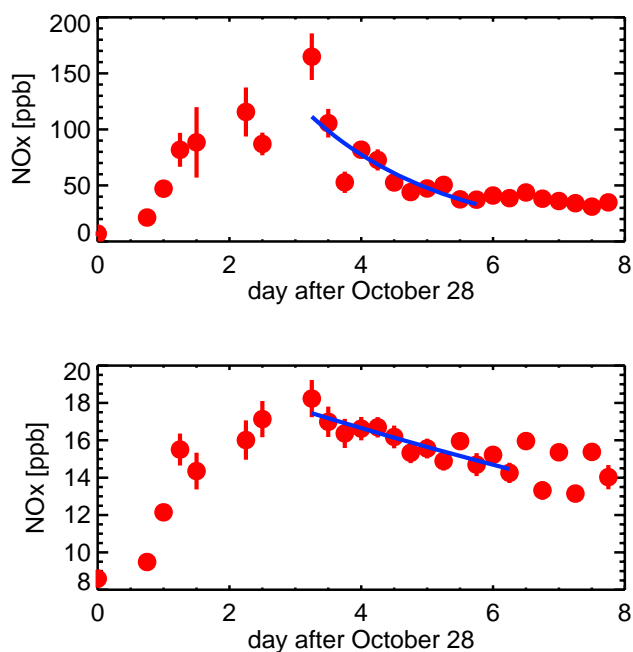
Fig. 1. MIPAS vmr measurements of NO$_x$ (red) at October–November 2003 and a fit of an exponential function (blue) between 50° S and 90° S and at 62 km (top) and 45 km (bottom) altitude. The error bars show the error of the mean of the zonal averages.

The following relation applies to the combined lifetime:

$$\frac{1}{\tau} = \frac{1}{\tau_{\text{phot}}} + \frac{1}{\tau_{\text{dyn}}}. \tag{3}$$

The photochemical lifetime of NO$_x$, τ_{phot}, can be calculated from the production of N(^{4}S) by NO photolysis and the loss of N(^{4}S) by Reaction (R6). This must be balanced by the competing reaction of N(^{4}S) with O$_2$ (Reaction R1), so τ_{phot} can be estimated as:

$$\tau_{\text{phot}} = \frac{1}{2 \cdot J_{\text{NO}} \cdot \text{br}_{\text{R6}}}. \tag{4}$$

br_{R6} denotes the branching ratio of Reaction (R6) compared with both reactions at which N(^{4}S) is a reactant (Reactions R1 and R6):

$$\text{br}_{\text{R6}} = \frac{k_{\text{R6}}[\text{NO}]}{k_{\text{R6}}[\text{NO}] + k_{\text{R1}}[\text{O}_2]}, \tag{5}$$

with $k_{\text{R1}} = 1.5 \times 10^{-11} \cdot e^{\frac{-3600}{T}}$, and $k_{\text{R6}} = 2.1 \times 10^{-11} \cdot e^{\frac{100}{T}}$ (Sander et al., 2006).

SLIMCAT (Chipperfield, 1999) calculates photolysis rates J_{NO}, for the corresponding times and geolocations of the observations, by interpolating precomputed J_{NO} of a four-dimensional (pressure, temperature, O$_3$ column and solar zenith angle) look-up table. The absorption cross section of NO is taken from Minschwaner and Siskind (1993). They

give an uncertainty of "30–40 % in the stratospheric photolysis rate". We get the NO number density and the temperature T from MIPAS data. For these calculations, we only use daytime data, so the calculated photochemical lifetimes are a lower limit. Thus the calculated dynamic lifetimes τ_{dyn} are an upper limit.

The lifetime τ, the photochemical lifetime τ_{phot}, and the dynamic lifetime τ_{dyn} are displayed in Fig. 2 (left) depending on the altitude. The errors specify the 1-σ range. The lifetimes τ, τ_{phot}, and τ_{dyn} decrease with increasing altitude. At 44 km τ is 20.6 ± 3.6 days and it decreases to the highest analyzed altitude at 64 km where it is only 1.8 ± 0.4 days. At 54 km altitude, there is a local maximum of the lifetimes. During the SPE, the polar vortex in the Southern Hemisphere was already gone, so it cannot be responsible. Nevertheless in these altitudes dynamical transport is apparently less effective. It also plays a role, that Reaction (R1) is more effective near the stratopause than at other altitudes due to the strong temperature-dependency. So N(^{4}S), which is produced by photolysis, prefers Reaction (R1) rather than Reaction (R6). The photochemical lifetime becomes shorter with increasing altitude. At 44 km τ_{phot} is 304 days, at 64 km only 4.2 days. This means at an altitude of 44 km J is 6 % of $\frac{1}{\tau}$, and at 64 km J is at 44 %.

3.2 Dependence of NO$_x$ on ion pair production

With estimates of NO$_x$ lifetimes available we can now analyze the relation between the number density n of NO$_x$ and the ion production rate due to the particle precipitation. n is calculated from the retrieved quantities T, p, and vmr. It is intended to reproduce a dependence of n on ion pair production.

We use MIPAS measurements only from 1 October 2003 until 31 March 2004 from latitudes 50–90° S and altitudes 44–62 km. The number density is derived every six hours from a running mean over the previous 24 h. As already discussed in the introduction, NO$_x$ is produced by SPEs through impact ionization/dissociation and ion chemistry. In addition, the temporal evolution of NO$_x$ is modulated by the lifetime τ of a NO$_x$-molecule. In the following, the production of NO$_x$ due to ionization will be described using MIPAS data. The difference of the number density of NO$_x$ affected by IPP due to energetic particle precipitation $n(\text{IPP}, t_0)$ and the background number density $n(\text{IPP} = 0, t_0)$ without particle precipitation at the time t_0 is

$$\Delta n_{\text{MIPAS}}(t_0) = n(\text{IPP}, t_0) - n(\text{IPP} = 0, t_0). \tag{6}$$

Consequently, $\Delta n_{\text{MIPAS}}(t_0)$ denotes the enhancement of n due to IPP. $n(\text{IPP}, t_0)$ can be determined by analyzing MIPAS data. $n(\text{IPP} = 0, t_0)$ is determined by means of a polynomial function, fitted to the MIPAS data. To do this reliably the period from 1 October 2003 until 31 March 2004 is fitted. Both $n(\text{IPP}, t_0)$ and $n(\text{IPP} = 0, t_0)$ are shown in Fig. 3 (left) as crosses and as a green graph, respectively, for altitudes
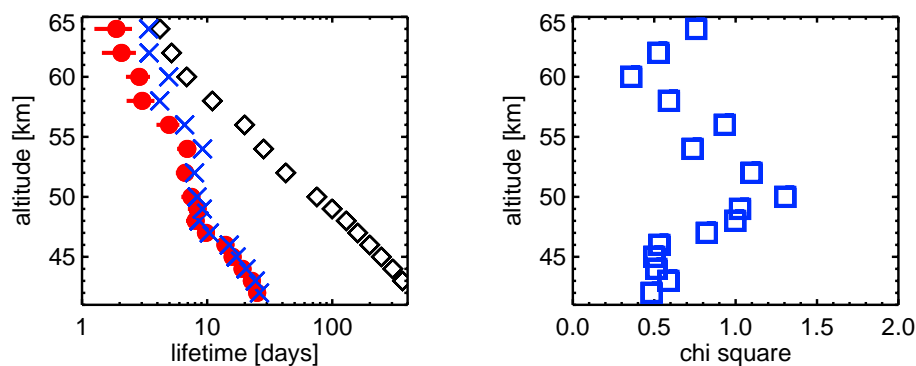
Fig. 2. Left: altitude-dependent lifetimes of NO$_x$ after the SPE at 30 October between 50° S and 90° S. The lifetimes τ as calculated from MIPAS measurements are displayed in red. The red error bars show the 1-σ range of the value. The photochemical lifetimes τ_{phot} are displayed in black diamonds. The resulting dynamic lifetimes τ_{dyn} are displayed in blue crosses. Right: altitude-dependent χ^2 values between measurement and fit of the exponential function according to the figures left.

of 45 km (bottom) and 56 km (top). The colour code of the crosses is time dependent: at days before the SPE the crosses are green and yellow. During the SPE they are orange and merge to red till the end of December. Days in 2004 are dark (black to blue).

A theoretical determination of the NO$_x$ number density enhancement requires the correct accumulation of the previous IPP, because the NO$_x$-lifetime τ is several days long (Sect. 3.1). The accumulated ion pair production $I(\text{IPP}, \tau, t_0)$ takes into account NO$_x$ loss processes by weighting the previous IPP with an exponential loss function depending on the quotient of the time difference $t_0 - t$ and the NO$_x$-lifetime τ:

$$I(\text{IPP}, \tau, t_0) = \int_{-\infty}^{t_0} \text{IPP}(t) \cdot e^{-\frac{t_0 - t}{\tau}} \, dt. \quad (7)$$

The enhancement of the NO$_x$ number density Δn_{theory} due to $I(\text{IPP}, \tau, t_0)$ at the time t_0 can thus be determined theoretically by assuming a production rate of 1.25 NO$_x$ per ion pair:

$$\Delta n_{\text{theory}}(\text{IPP}, \tau, t_0) = 1.25 \cdot \frac{\text{NO}_x}{\text{ion pair}} \cdot I(\text{IPP}, \tau, t_0). \quad (8)$$

The AIMOS database (Sect. 2.2) provides IPP(t), τ was determined in Sect. 3.1. In order to examine whether the measured enhancement of the NO$_x$ number density Δn_{MIPAS} can be determined by $I(\text{IPP}, \tau, t_0)$, Eq. (8) is modified to

$$\Delta n_{\text{MIPAS}}(\text{IPP}, \tau, t_0) = x \cdot \frac{\text{NO}_x}{\text{ion pair}} \cdot I(\text{IPP}, \tau, t_0). \quad (9)$$

x is the altitude-dependent effective production rate of NO$_x$ per ion pair replacing the theoretical value of 1.25, and is empirically determined in the following. x is independent of the NO$_x$ lifetime, particularly.

In Fig. 3 (right) $\Delta n_{\text{MIPAS}}(t_0)$ is plotted over $I(\text{IPP}, \tau, t_0)$ at altitudes of 45 km (bottom) and 56 km (top). Only days of strong relevance are plotted (25 October–31 December 2003). It reveals, as expected, that $\Delta n_{\text{MIPAS}}(t_0)$ increases with $I(\text{IPP}, \tau, t_0)$. The black curves represent the theoretical trend with an effective NO$_x$-production rate of 1.25. The green curves represent the relation described by Eq. (9) with x fitted to the distribution.

At the days before the SPE (yellow crosses), the ion pair production increases, n does not, however. This means that AIMOS shows enhanced ionization rates on 28 October, but MIPAS does not show enhanced NO$_x$ volume mixing ratios. Ionization rates of these days are due to electrons and probable contamination by protons (Yando et al., 2011), and thus the ionization rates might be overestimated. There is another noticeable discrepancy at 56 km altitude regarding the NO$_x$-enhancement after 20 November (indicated by orange symbols). At these days, more NO$_x$ is produced than predicted by theory. Even an effective NO$_x$-production rate of 1.25 NO$_x$ per ion pair underestimates the measured NO$_x$ production. Either the effective production rate of NO$_x$ is higher under the particular conditions of the 20 November or the lifetime of NO$_x$ became significantly longer (altitude-dependent up to a factor 1.5).

The empirically determined altitude-dependent effective production rates are shown in Fig. 4 (left). The green error bars show the 1-σ uncertainties of the empirically determined effective NO$_x$-production rates per ion pair x. The altitude-dependent reduced residuals (χ^2) of the fits is shown in the right-hand figure. Most of the χ^2 values are significantly larger than one. Higher χ^2 values argue for a poorer fit and thus for a non-linear NO$_x$-production. The higher the NO$_x$ number density the less effective the NO$_x$-production becomes, which was already shown in Funke et al. (2011).

The effective NO$_x$-production rate is significantly lower than the initial N-production rate 1.25 at all altitudes. This is due to the fact, that the effective NO$_x$-production rate
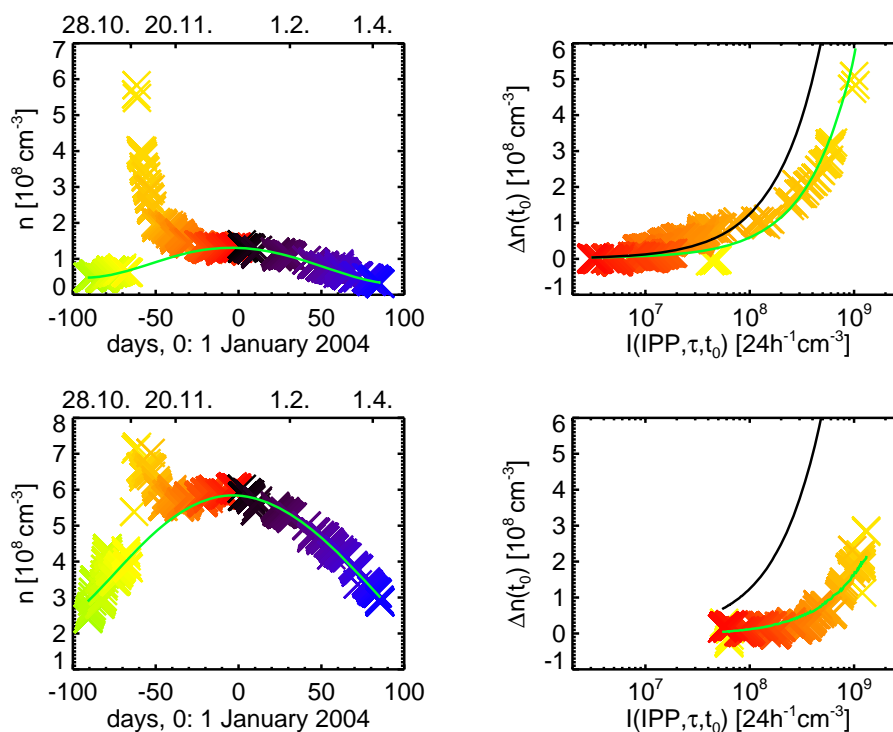
Fig. 3. Left: time curve of the number density n of NO_x at a geomagnetic latitudes between $50° $ S and $90°$ S, and at altitudes of 56 km (top) and 45 km (bottom) in the Austral summer 2003/04. The colour code of the crosses is time dependent: at days before the SPE, the crosses are green and yellow. During the SPE they are orange and merge to red until the end of December. Days in 2004 are dark (black to blue). The green curve is a fitted polynomial function and shows the background number density $n(\text{IPP} = 0)$. Right: Δn_{MIPAS} (the difference of the number density and the correspondent value of the fitted function at the plot left) is plotted in dependence of $I(\text{IPP}, \tau, t_0)$, specified in Eq. (7), at geomagnetic latitudes between $50°$ S and $90°$ S, and at altitudes of 56 km (top) and 45 km (bottom). The colour code is the same as in the left panel. The green curve is a linear fit. The black curve shows the theoretical function for a production rate of 1.25 N per ion pair. The standard error of the mean of the number densities is always lower than $1\,\%$, besides the days during the SPE (lower than $5\,\%$).

considers not only the production of $N(^4S)$ and $N(^2D)$ but also the fast chemical loss of $N(^4S)$ by Reaction (R6), which is already shown in Eq. (1). Slower dynamical or photochemical NO_x-loss processes are taken into account by $I(\text{IPP}, \tau, t_0)$ which is dependent on τ (Eq. 7), and thus, they do not influence the difference between the initial N-production rate and the effective NO_x-production rate x.

4 Comparison with previous model studies

Hereafter, the results from Sect. 3.2 are compared with the model studies of Funke et al. (2011) and Baumgaertner et al. (2010).
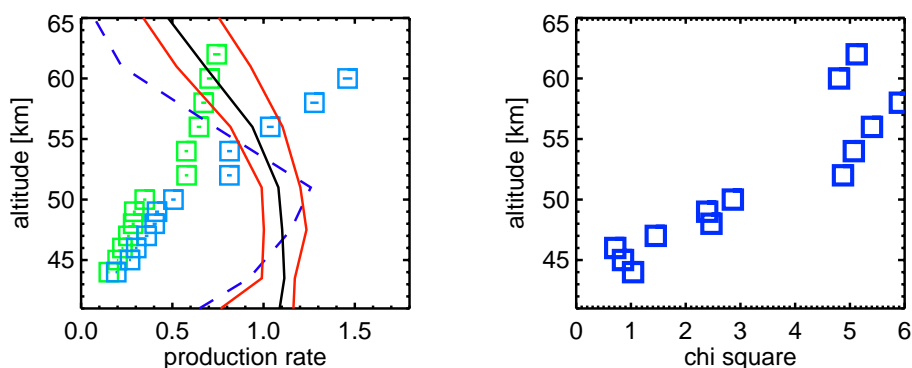
4.1 Funke et al. (2011)

In the High Energy Particle Precipitation in the Atmosphere (HEPPA) intercomparison the ability of numerous models to simulate atmospheric composition changes after the Halloween SPE was investigated (Funke et al., 2011). All involved models show a NO_y increase between 1.5 hPa and

0.4 hPa (~ 45–55 km), which is systematically higher than the increase measured by MIPAS. The authors give two different reasons for that. First, the ionization rates provided by AIMOS may be too high for these altitudes. Uncertainties of the satellite measurements of the electrons with an energy range of 300 keV–2.5 MeV and the extension to 5 MeV based on these measurements are rather high and may cause an overestimation of the ionization rates. Also, models using a family approach for NO_x tend to overestimate the net NO_x production.

Reaction (R1) strongly depends on temperature and the initial NO_y abundance. To demonstrate this, the authors show the production rate efficiency of NO_x (ratio of the net NO_x increase and the integrated initial N production) for the Northern Hemisphere during 28 October–1 November determined by a box model. The model considers temperature, Reactions (R1), (R2), (R3)-(R6), and following reactions:

$$NO_2 + O \rightarrow NO + O_2 \tag{R7}$$

$$N(^4S) + NO_2 \rightarrow N_2O + O \tag{R8}$$

$$NO_2 + O_3 \rightarrow NO_3 + O_2 \tag{R9}$$

Fig. 4. Left: the effective NO$_x$-production rate per ion pair x in dependence of the altitude at a geomagnetic latitudes between 50° S and 90° S. x (green symbols) is the gradient of the fit shown as green line in Fig. 3 (right panel). The blue symbols show x calculated without electron ionization rates. The error bars show the 1-σ range of the effective production rates. The black curve shows the effective daytime NO$_x$-production rate per ion pair, calculated with a box model. The red curves show the error range after varying the initial values of this box model as described in Sect. 4.1. The violet dashed curve shows the effective daytime NO$_x$-production rate, calculated with the initial N- and NO-production rates determined by Baumgaertner et al. (2010). Right: the altitude-dependent reduced residual χ^2 of the fits related to the green line in Fig. 3 (right panel) corresponding to the green symbols (left).

$$NO_3 + NO \rightarrow 2 \cdot NO_2 \tag{R10}$$

$$O + O_2 \rightarrow O_3 \tag{R11}$$

$$NO_2 + NO_3 \rightarrow N_2O_5. \tag{R12}$$

In addition the box model accounts for ionization rates. Transport is not considered, but this should be of no consequence as mentioned above, because in our determination of the effective production rates in Sect. 3.2, loss processes due to transport are taken into account with $I(\text{IPP}, \tau, t_0)$ depending on τ (Eq. 7).

We used the same box model to test the dependence of the effective production. But we used other initial values for the Southern Hemisphere namely temperature, NO, NO$_2$, O$_3$, measured by MIPAS, the ionization rates of AIMOS and the photolysis rates of SLIMCAT. In Fig. 4 (left) the black curve shows the result of this box model. The red curves show the estimated error range after varying the initial values (temperature: ± 10 K and NO, NO$_2$, O$_3$: ± 10 %). The shape of the black curve is explained by Reaction (R1) which is strongly temperature-dependent. It is less effective in colder and therefore higher altitudes in the mesosphere. Compared to the Northern Hemisphere (i.e. Funke et al., 2011), the Southern Hemisphere is 60 °K warmer at 40 km (3 hPa) altitude and 40 °K at 50 km (1 hPa). At 60 km (0.2 hPa), there is no big difference in temperature. The effective NO$_x$-production rates of the box model, labelled here as ENP_P, are considerably higher at lower altitudes. The difference ranges from from 7.5 times at 44 km to 1.5 times at 56 km. At higher altitudes the error bars of the measured and modelled effective NO$_x$-production rates overlap. The discrepancies between measured and modelled effective NO$_x$-production rates at altitudes between 44 km to 52 km are only

in qualitative accordance to the results of the HEPPA intercomparison. The discrepancies in that intercomparison are much lower. Because electron ionization rates are probably contaminated by protons, we did a test using ionization rates due to precipitating protons and their secondaries only (blue symbols). It showed that the discrepancy cannot be explained only by this effect, which is also only qualitative in accordance to the WACCMp model run of their study.

The high discrepancies between theoretical and empirically determined values can be composed of different error sources:

– Systematic NO$_x$ retrieval errors up to 15 % (Sect. 2.1).

– Production rates of high energetic electrons are overestimated. We did the same calculation without electron ionization (blue squares, Fig. 4, left). Between 58 km and 62 km altitude, electron ionization is needed. Between 52 km and 56 km this effect could explain the discrepancies and between 44 km and 50 km altitude this effect could only explain between 5 % and 25 % of the discrepancies.

– Calculations with a shorter lifetime (-33 %) lead to a higher effective production rate (about 30 %).

Known error sources can explain the discrepancies between 52 km and 62 km. To explain the discrepancies for altitudes between 44 km and 50 km, a change in the proton ionization rates, in the N-production rate, or in the N(^{2}D)-N(^{4}S)-branching ratio is needed.

4.2 Baumgaertner et al. (2010)

In their study, Baumgaertner et al. (2010) only accounted for the proton flux, measured by GOES. In a first run, they start

with a production rate of 0.55 N(^{4}S) and 0.7 N(^{2}D), resulting in the production of NO, per ion pair. Results of the ECHAM/MESSy Atmospheric Chemistry (EMAC) model are compared with measurements of MIPAS. The mesospheric enhancement of NO_2 is lower in the measurement (50 ppbv) than in the simulation (60 ppbv). However, the difference can be explained by systematic errors and dynamical effects. In order to improve the simulated N_2O abundance, which is seven times higher than the measured one, tests with alternative altitude-dependent N- and NO-production rates (each between 0 and 1.2) were performed. Baumgaertner et al. (2010) present in Fig. 9 the N- and NO-production rates, which fitted best.

We used these altitude dependent N- and NO-production rates to calculate effective NO_x-production rates ENP_B with the box model, described in Sect. 4.1. This is shown as a violet dashed line in Fig. 4 (left). Differences to ENP_P (black line) are only caused by the differences due to the altitude-independent NO_x-production rate of Porter et al. (1976). These differences do not show a clear approximation to the effective NO_x-production rates x calculated in Sect. 3.2. ENP_B are considerably higher than x at altitudes from 44 km to 54 km (factor 2–5) and significantly lower at 60 km and 62 km (factor 0.3–0.4). At 56 km and 58 km altitude error bars overlap. These differences most likely have different reasons. The authors fit the N_2O abundance, while in our study, the NO_x abundance is fitted. This can lead to discrepancies. Then, they looked at the Northern Hemisphere, which has other conditions regarding temperature, dynamics, and gas abundances as the Southern Hemisphere. Finally, they do not account for dynamics, but this should be of no consequence, because due to Eq. (7), loss processes (dynamical and photochemical) are taken into account in our calculations.

5　Conclusions

We have derived effective NO_x-production rates and NO_x lifetimes directly from the measurement, in order to provide model diagnostics.

We showed a simple method to derive lifetimes of NO_x after a solar proton event by means of MIPAS/ENVISAT measurements. The lifetime of NO_x at that time, at altitudes between 44 km and 64 km mainly depends on dynamic effects and less on photochemistry, because in most cases the lifetime of NO_x is significantly shorter than the sole photochemical lifetime. Including the lifetime of NO_x, we were able to calculate the dependence of the effective NO_x-production on the ion pair production. The calculated effective NO_x-production rates do not reproduce the theoretical value of 1.25 due to chemical loss processes of NO_x.

The effective NO_x-production rate and the NO_x-lifetime we determined can be used as model diagnostics for model-measurement comparison. We compared the effective NO_x-

production rates with those calculated with a box model by Funke et al. (2011). Between 54 km and 62 km altitude, differences between the inferred and calculated effective production rates are within the estimated error. But at altitudes between 44 km and 52 km, the measured production rates are significant lower than in the box model. At the same altitudes, the models of the HEPPA intercomparison show a too high NO_x-production. We showed that precipitating energetic electrons can be an error source, but not the only one. Ionization rates due to protons are possibly overestimated at these altitudes as well.

Edited by: A. Geer

References

Baumgaertner, A. J. G., Jöckel, P., Riede, H., Stiller, G., and Funke, B.: Energetic particle precipitation in ECHAM5/MESSy – Part 2: Solar proton events, Atmos. Chem. Phys., 10, 7285–7302, doi:10.5194/acp-10-7285-2010, 2010.

Brasseur, G. P. and Solomon, S.: Aeronomy of the Middle Atmosphere, 3rd ed., Springer, Dordrecht, the Netherlands, 2005.

Chipperfield, M. P.: Multiannual simulations with a three-dimensional chemical transport model, J. Geophys. Res., 104, 1781–1805, 1999.

Crutzen, P. J., Isaksen, I. S. A., and Reid, G. C.: Solar proton events – Stratospheric sources of nitric oxide, Science, 189, 457–459, doi:10.1126/science.189.4201.457, 1975.

Fischer, H., Birk, M., Blom, C., Carli, B., Carlotti, M., von Clarmann, T., Delbouille, L., Dudhia, A., Ehhalt, D., Endemann, M., Flaud, J. M., Gessner, R., Kleinert, A., Koopman, R., Langen, J., López-Puertas, M., Mosner, P., Nett, H., Oelhaf, H., Perron, G., Remedios, J., Ridolfi, M., Stiller, G., and Zander, R.: MIPAS: an instrument for atmospheric and climate research, Atmos. Chem. Phys., 8, 2151–2188, doi:10.5194/acp-8-2151-2008, 2008.

Funke, B., López-Puertas, M., von Clarmann, T., Stiller, G. P., Fischer, H., Glatthor, N., Grabowski, U., Höpfner, M., Kellmann, S., Kiefer, M., Linden, A., Mengistu Tsidu, G., Miliz, M., Steck, T., and Wang, D. Y.: Retrieval of stratospheric NO_x from 5.3 and 6.2 μm nonlocal thermodynamic equilibrium emissions measured by Michelson Interferometer for Passive Atmospheric Sounding (MIPAS) on Envisat, J. Geophys. Res., 110, D09302, doi:10.1029/2004JD005225, 2005.

Funke, B., López-Puertas, M., Gil-López, S., von Clarmann, T., Stiller, G. P., Fischer, H., and Kellmann, S.: Downward transport of upper atmospheric NO_x into the polar stratosphere and lower mesosphere during the Antarctic 2003 and Arctic 2002/2003 winters, J. Geophys. Res., 110, D24308, doi:10.1029/2005JD006463, 2005.

Funke, B., Baumgaertner, A., Calisto, M., Egorova, T., Jackman, C. H., Kieser, J., Krivolutsky, A., López-Puertas, M., Marsh, D. R., Reddmann, T., Rozanov, E., Salmi, S.-M., Sinnhuber, M., Stiller, G. P., Verronen, P. T., Versick, S., von Clarmann, T., Vyushkova, T. Y., Wieters, N., and Wissing, J. M.: Composition changes after the "Halloween" solar proton event: the High Energy Particle Precipitation in the Atmosphere (HEPPA) model versus MIPAS data intercomparison study, Atmos. Chem. Phys., 11, 9089–9139, doi:10.5194/acp-11-9089-2011, 2011.

Jackman, C. H., McPeters, R. D., Labow, G. J., Fleming, E. L., Praderas, C. J., and Russell, J. M.: Northern hemisphere atmospheric effects due to the July 2000 solar proton event, Geophys. Res. Lett., 28, 2883–2886, 2001.

Jackman, C. H., DeLand, M. T., Labow, G. J., Fleming, E. L., Weisenstein, D. K., Ko, M. K. W., Sinnhuber, M., and Russell, J. M.: Neutral atmospheric influences of the solar proton events in October–November 2003, J. Geophys. Res., 110, A09S27, doi:10.1029/2004JA010888, 2005

Jackman, C. H., Roble, R. H., and Fleming, E. L.: Mesospheric dynamical changes induced by solar proton events in October–November 2003, Geophys. Res. Lett., 34, L04812, doi:10.1029/2006GL028328, 2007.

Jackman, C. H., Marsh, D. R., Vitt, F. M., Garcia, R. R., Fleming, E. L., Labow, G. J., Randall, C. E., López-Puertas, M., Funke, B., von Clarmann, T., and Stiller, G. P.: Short- and medium-term atmospheric constituent effects of very large solar proton events, Atmos. Chem. Phys., 8, 765–785, doi:10.5194/acp-8-765-2008, 2008.

López-Puertas, M., Funke, B., Gil-López, S., von Clarmann, T., Stiller, G. P., Höpfner, M., Kellmann, S., Fischer, H., and Jackson, C. H.: Observations of NO_x-Enhancements and Ozone Depletion in the Northern and Southern Hemispheres after the October–November 2003 Solar Proton Events, J. Geophys. Res., 110, A09S44, doi:10.1029/2005JA011050, 2005.

Minschwaner, K. and Siskind, D. E.: A New Calculation of Nitric Oxide Photolysis in the Stratosphere, Mesosphere, and Lower Thermosphere, J. Geophys. Res., 98, 20401–20412, 1993.

Porter, H. S., Jackman, C. H., and Green, A. E. S.: Efficiencies for production of atomic nitrogen and oxygen by relativistic proton impact in air, J. Chem. Phys., 65, 154–167, doi:10.1063/1.432812, 1976.

Randall, C. A., Harvey, V. L., Singleton, C. S., Bailey, S. M., Bernath, P. F., Codrescu, M., Nakajima, H., and Russell III, J. M.: Energetic particle precipitation effects on the Southern Hemisphere stratosphere in 1992–2005, J. Geophys. Res., 112, D08308, doi:10.1029/2006JD007969, 2007.

Rusch, D. W., Gerard, J.-C., Solomon, S., Crutzen, P. J., and Reid, G. C.: The effect of particle precipitation events on the neutral and ion chemistry of the middle atmosphere – I. odd nitrogen, Planet. Space Sci., 29, 767–774, 1981.

Sander, S. P., Friedl, R. R., Ravishankara, A. R., Golden, D. M., Kolb, C. E., Kurylo, M. J., Molina, M. J., Moortgat, G. K., Keller-Rudek, H., Finlayson-Pitts, B. J., Wine, P., Huie, R. E., and Orkin, V. L.: Chemical kinetics and Photochemical Data for the Use in Atmospheric Studies. Evaluation Number 15, JPL publication 06-2, Jet Propulsion Laboratory, California Institute of Technology, Pasadena, CA, 2006.

Seppälä, A., Verronen, P. T., Kyrölä, E., Hassinen, S., Backman, L., Hauchecorne, A., Bertaux, J. L., and Fussen, D.: Solar proton events of October-November 2003: Ozone depletion in the Northern Hemisphere polar winter as seen by GOMOS/Envisat, Geophys. Res. Lett., 31, L19107, doi:10.1029/2004GL021042, 2004.

Seppälä, A., Cliverd, M. A., and Rodger, C. J.: NO_x enhancements in the middle atmosphere during 2003-2004 polar winter: Relative significance of solar proton events and the aurora as a source, J. Geophys. Res., 112, D23303, doi:10.1029/2006JD008326, 2007.

Sinnhuber, M., Nieder, H., and Wieters, N.: Energetic Particle Precipitation and the Chemistry of the Mesosphere/Lower Thermosphere, Surv. Geophys., Springer, doi:10.1007/s10712-012-9201-3, 2012.

Siskind, D. E. and Russell III, J. M.: Coupling between middle and upper atmospheric NO: Constraints from HALOE observations, Geophys. Res. Lett., 27, 329–332, doi:10.1029/1999GL010940, 1996.

Toohey, M., von Clarmann, T., Hegglin, M., Tegtmeier, S., and the SPARC Data Initiative team: SPARC Data Initiative: climatology uncertainty assessment, World Climate Research Programme, Open Science Conference, Denver, 2011.

Wissing, J. M. and Kallenrode, M.-B.: Atmospheric Ionization Module Osnabrück (AIMOS): A 3-D model to determine atmospheric ionization by energetic particles from different populations, J. Geophys. Res., 115, A06104, doi:10.1029/2008JA013884, 2009.

Yando, K., Millan, R. M., Green, J. C., and Evans, D. S.: A Monte Carlo simulation of the NOAA POES Medium Energy Proton and Electron Detector instrument, J. Geophys. Res., 116, A10231, doi:10.1029/2011JA016671, 2011.